

Enhanced Superconductivity at Quantum-Critical KTaO_3 Interfaces

Jieun Kim^{1,†}, Muqing Yu^{2,†}, Ahmed Omran², Jiangfeng Yang¹, Ranjani Ramachandran², William O. Nachlas³, Patrick Irvin², Jeremy Levy^{2,*} and Chang-Beom Eom^{1,*}

¹Department of Materials Science and Engineering, University of Wisconsin-Madison, Madison, 53706, Wisconsin, USA.

²Department of Physics and Astronomy, University of Pittsburgh, Pittsburgh, 15260, Pennsylvania, USA.

³Department of Geoscience, University of Wisconsin-Madison, Madison, 53706, Wisconsin, USA.

†These authors contributed equally to this work.

*Corresponding author(s). E-mail(s): jlevy@pitt.edu; ceom@wisc.edu;

Abstract

Superconductivity at oxide interfaces has intrigued researchers for decades, yet the underlying pairing mechanism remains elusive. Here we demonstrate that proximity to a ferroelectric quantum critical point dramatically enhances interfacial superconductivity in KTaO_3 . By precisely tuning KTaO_3 to its quantum critical composition through 0.8% niobium doping, we achieve a near-doubling of the superconducting transition temperature, reaching 2.9 K. Remarkably, a dome-shaped carrier density dependence emerges exclusively at the quantum critical point, contrasting sharply with the linear scaling observed in undoped interfaces. Our findings establish ferroelectric quantum criticality as a powerful mechanism for enhancing superconductivity and provide compelling evidence for soft-phonon-mediated pairing in these systems.

Keywords: quantum criticality, 2D superconductivity, soft phonons, oxide interfaces

Introduction

Oxide interfaces represent a frontier in condensed matter physics, hosting emergent phenomena absent in their bulk counterparts^{1–3}. Among these systems, two-dimensional electron gases at the interface of insulating oxides, such as $\text{LaAlO}_3/\text{SrTiO}_3$ and $\text{LaAlO}_3/\text{KTaO}_3$, have been a subject of intense research due to their surprising metallic and superconducting properties. The existence of superconductivity in these systems is puzzling, given their extremely low carrier densities and exceptionally low superconducting transition temperatures (T_c).

A particularly intriguing puzzle arises when comparing the magnitudes of T_c in SrTiO_3 and KTaO_3 . While both are incipient ferroelectrics KTaO_3 interfaces achieve higher superconducting transition temperatures than SrTiO_3 interfaces^{1,3}, despite SrTiO_3 being closer to ferroelectric instability^{4,5}. Furthermore, KTaO_3 -based interfaces exhibit superconductivity, only at specific crystallographic orientations^{3,6–11} and shows anomalous carrier density scaling^{6,10}. These paradoxes suggest a fundamental gap in our understanding of the pairing mechanism. While quantum criticality drives superconductivity by providing the pairing glue for electrons in unconventional superconductors^{12–16}, its role in oxide interfaces remains largely unexplored.

Recent theoretical work by Edge et al.¹⁷ provides a framework to resolve this paradox¹⁷. Their model suggests that the superconducting dome observed in SrTiO_3 originates from a competition between the emergence of a Fermi surface and the carrier-induced suppression of ferroelectric quantum fluctuations. KTaO_3 offers an ideal platform to investigate this connection: quantum fluctuations suppress its expected ferroelectric transition, maintaining cubic symmetry to absolute zero¹⁸. This places KTaO_3 in the ideal regime to test the hypothesis that ferroelectric quantum criticality can enhance pairing through soft phonon fluctuations. Crucially, Nb substitution tunes $\text{KTa}_{1-x}\text{Nb}_x\text{O}_3$ precisely to a ferroelectric quantum critical point at a well-defined, low Nb content ($x = 0.8\%$ ¹⁹). At this composition, quantum fluctuations, and therefore any phonon-mediated enhancement of pairing, are expected to maximize.

Here we systematically explore how proximity to the quantum critical point governs interfacial superconductivity in Nb-doped KTaO_3 , revealing a profound enhancement mechanism linked to soft phonon dynamics. To isolate quantum criticality effects from disorder effects, we combine electrostatic gating with adsorption-controlled epitaxial growth with precise control of K stoichiometry and Nb content. Electronic grade Nb-doped KTaO_3 films and atomically clean $\text{LaAlO}_3/\text{KTa}_{1-x}\text{Nb}_x\text{O}_3$ interfaces reduce disorder and stabilize the (111) orientation where superconductivity is most robust²⁰. This platform allows quantitative links to be established between transport, carrier density, and soft mode tuning, and it separates intrinsic quantum critical responses from extrinsic effects that often mask narrow composition windows.

Results

Quantum critical enhancement of superconductivity

We performed transport measurements to examine how Nb doping affects interfacial superconductivity by growing epitaxial $\text{KTa}_{1-x}\text{Nb}_x\text{O}_3$ thin films with four precisely controlled compositions spanning the quantum critical point: $x = 0, 0.4\%, 0.8\%$, and 1.6% . All films are grown on (111)-oriented KTaO_3 substrates with amorphous LaAlO_3 overlayers to create conducting interfaces using a recently developed hybrid pulsed laser deposition

technique²⁰ (see Methods). The temperature dependence of the sheet resistance (R_{sq}) of the films, measured over the entire surface of the films in a Van der Pauw geometry, shows metallic behavior for all films, demonstrating high-quality epitaxial growth of the $\text{KTa}_{1-x}\text{Nb}_x\text{O}_3$ films with precise K stoichiometry²⁰. To isolate quantum criticality effects from sheet carrier density (n_{2D}) variations, we select samples with comparable n_{2D} values at low temperatures (Fig. 1b). The Nb-doped samples have $n_{2D} = 5.6\text{-}6.0 \times 10^{13} \text{ cm}^{-2}$ at 4 K, while the undoped sample has $n_{2D} = 8.11 \times 10^{13} \text{ cm}^{-2}$. We patterned Hall bars along the [11-2] and determined the superconducting transition temperature T_c at 50% of the normal state R_{sq} , just above the transition. The R_{sq} drops to zero for all samples, attesting to the quality of the $\text{LaAlO}_3/\text{KTa}_{1-x}\text{Nb}_x\text{O}_3$ (111) interfaces with minimal growth-induced disorder and to the resultant uniformity of the superconducting phase. Remarkably, the Nb-doped samples exhibit enhanced T_c (2.05-2.5 K) compared to the undoped sample (1.53 K), despite their lower n_{2D} (Fig. 1c). Both T_c and critical current density (J_c) peak precisely at $x = 0.8\%$ (insets of Fig. 1c,d), corresponding to the known bulk ferroelectric quantum critical point¹⁹. This striking correlation demonstrates that quantum criticality, not carrier density, drives the enhancement.

Emergence of a superconducting dome

Having established enhancement of T_c at the quantum critical point, we explore how carrier density affects this phenomenon in $\text{LaAlO}_3/\text{KTa}_{0.992}\text{Nb}_{0.008}\text{O}_3$ (111) interfaces. By varying the LaAlO_3 growth temperature (T_g) from 100 to 500 °C, we can systematically tune n_{2D} of $\text{LaAlO}_3/\text{KTa}_{0.992}\text{Nb}_{0.008}\text{O}_3$ (111) from 4.67 to $7.48 \times 10^{13} \text{ cm}^{-2}$ ¹². The resulting distributions of n_{2D} and mobility (μ) at 10 K (Fig. 2a) show that the mobility distribution is shifted to lower values in the Nb-doped samples compared to the undoped samples. This shift is consistent with additional impurity scattering introduced by dilute Nb dopants but it evolves smoothly with n_{2D} and does not produce a peak that could mimic the non-monotonic T_c . Figure 2b reveals a non-monotonic dependence of T_c on n_{2D} , with a maximum of 2.9 K at $n_{2D} = 6.35 \times 10^{13} \text{ cm}^{-2}$ - nearly double the value for undoped interfaces. Systematic measurements on 20 samples reveal a striking dome-shaped dependence at the quantum critical point (Fig. 2c), contrasting sharply with the linear relationship in undoped KTaO_3 ⁷.

Electrostatic gate tuning at the quantum critical composition

The superconducting dome in $\text{LaAlO}_3/\text{KTa}_{0.992}\text{Nb}_{0.008}\text{O}_3$ (111) interfaces is confirmed not only by varying the n_{2D} using different LaAlO_3 growth temperatures, but also by directly modulating the n_{2D} at the quantum critical composition. Due to the relatively low $\delta n_{2D} (< 2 \times 10^{13} \text{ cm}^{-2})$ that can be induced by electrostatic gating in KTaO_3 and the large range of n_{2D} where KTaO_3 is superconducting ($\approx 10^{14} \text{ cm}^{-2}$), we chose three samples prepared with $T_g = 250, 475, 550$ °C, which represent $\text{LaAlO}_3/\text{KTa}_{0.992}\text{Nb}_{0.008}\text{O}_3$ (111) interfaces with carrier densities in the under-doped, optimally-doped, and over-doped regimes, respectively. Fig. 3a shows the R_{sq} (T) along the [11-2] for the 475 °C sample. At $V_G = 0$ V, the superconducting transition occurs at $T_c = 2.9$ K. Sweeping V_G from -26 to 120 V shifts the entire transition while the ground state remains at zero resistance, indicating a strong V_G dependence of T_c . Fig. 3b shows the modulation of n_{2D} and μ for the 250, 475, 550 °C samples. For all samples, n_{2D} and μ decrease monotonically as V_G is lowered from 50 V to -50 V, as expected from enhanced effective disorder near the interface. In contrast to the monotonic decrease in n_{2D} , we observe contrasting evolution of T_c with V_G (Fig. 3c). In the 250 °C sample, T_c shows nearly monotonic decrease as V_G is lowered whereas in the 475 °C sample T_c initially increases to a peak of 3.0 K before decreasing as n_{2D} passes the top of the superconducting dome at $n_{2D} = 5.39 \times 10^{13} \text{ cm}^{-2}$. In the 550 °C sample, T_c

exhibits a strongly inverse correlation with n_{2D} , as expected in the over-doped regime. Taken together, the 250, 475, 550 °C samples map a nearly continuous superconducting dome in the T_c - n_{2D} diagram. The 250 °C and 550 °C samples occupy the low and high n_{2D} sides and trace the rising and falling branches, respectively, while the 475 °C samples connect the two branches, with the apex located near $n_{2D} = 5.39 \times 10^{13} \text{ cm}^{-2}$ and $T_c = 3.0 \text{ K}$. Over the same n_{2D} range, the undoped KTaO_3 reference increases approximately linearly with and shows no maximum. Collectively, these results establish a non-monotonic dependence of T_c on n_{2D} at the ferroelectric quantum critical point.

Discussion

The substantial enhancement of superconductivity at the ferroelectric quantum critical point reveals a fundamental connection between quantum lattice fluctuations and Cooper pair formation in $\text{LaAlO}_3/\text{KTa}_{0.992}\text{Nb}_{0.008}\text{O}_3$ (111) interfaces. Unlike conventional phonons, whose occupation is thermally suppressed at low temperatures, quantum critical polar fluctuations persist down to absolute zero. These fluctuations provide an unusually robust pairing channel, explaining why T_c nearly doubles despite reduced carrier density relative to undoped KTaO_3 interfaces. Our results therefore provide compelling evidence for a long-standing hypothesis: the soft-phonon-mediated pairing can dominate in oxide superconductors when a ferroelectric mode is tuned to criticality.

The emergence of a dome-shaped dependence of T_c on n_{2D} reinforces this mechanism. In undoped KTaO_3 , T_c scales linearly with n_{2D} , consistent with conventional BCS behavior where a growing Fermi surface expands the phase space for electron-phonon interaction. At the quantum critical composition, however, this linearity breaks down and T_c first rises at low n_{2D} as polar fluctuations strongly enhance pairing, but at higher n_{2D} these fluctuations are progressively screened by mobile carriers, resulting in an optimal density and a dome-shaped profile in the T_c - n_{2D} diagram. This non-monotonicity mirrors that observed in doped SrTiO_3 and in a wide range of unconventional superconductors near nematic or magnetic quantum critical points, highlighting the universality of quantum criticality as a driver of superconductivity^{15,17,21}. We note that the emergence of a superconducting dome at the quantum critical point in the regime of linear dependence of T_c on n_{2D} leads to highly anisotropic enhancement of T_c on either side of the dome. On the over-doped side, T_c collapses rapidly to that of the undoped baseline within $\delta n_{2D} \approx 1.8 \times 10^{13} \text{ cm}^{-2}$ beyond the peak, whereas the under-doped side exhibits a three-fold enhancement of T_c even at $\delta n_{2D} \approx 2.1 \times 10^{13} \text{ cm}^{-2}$. These quantitative comparisons demonstrate that quantum critical polar fluctuations enhance superconductivity over a broad under-doped range, whereas their carrier-induced screening at high n_{2D} sharply suppresses the enhancement. This asymmetry distinguishes the superconducting dome at the ferroelectric quantum critical point in KTaO_3 from the more symmetric superconducting domes found in SrTiO_3 , cuprates, and iron pnictides near their quantum criticalities^{15,22,23}, underpinning the pronounced role of polar fluctuations in this system. At the same time, the observation that T_c peaks precisely at the ferroelectric quantum critical point establishes the general framework for soft-phonon-mediated superconductivity put forward by earlier theoretical¹⁷ and experimental works, opening the door to engineering similar enhancements of superconductivity in other quantum paraelectric and correlated systems near structural or magnetic quantum critical points.

Future experiments could directly probe soft phonon spectra at these interfaces using inelastic neutron scattering or ultrafast spectroscopy, which will be essential for quantifying

the dynamics of the critical mode and its coupling to the superconducting condensate²⁴⁻²⁹. The interplay between strong Rashba spin-orbit coupling in KTaO_3 ³⁰ and quantum critical superconductivity may enable exotic phases including topological superconductivity. Finally, our ability to position electronic-grade KTaO_3 precisely at its ferroelectric quantum critical point by Nb doping underlines the promise of advanced synthesis approaches. Continued progress in adsorption-controlled epitaxy and related techniques^{20,31,32} will expand the accessible phase space for volatile-refractory systems and correlated oxides, enabling systematic exploration of structural, magnetic, and electronic quantum criticalities. The nearly two-fold enhancement of T_c achieved here illustrates how synthesis-driven access to critical regimes can serve as a powerful lever for engineering superconductivity, and bodes well for future advances in the design of next-generation quantum materials with tunable and enhanced functionalities.

Methods

Film synthesis and structural characterization

Epitaxial $\text{KTa}_{1-x}\text{Nb}_x\text{O}_3$ thin films were grown using hybrid pulsed laser deposition (PLD) combining a KrF excimer laser (248 nm) with an effusion cell for potassium delivery. Films were deposited on (111)-oriented KTaO_3 substrates at 973 K in 10^{-6} Torr. Ceramic targets of $(1-x)\text{Ta}_2\text{O}_5-x\text{Nb}_2\text{O}_5$ ($x = 0, 0.004, 0.008, 0.016$) were ablated at 0.5 J/cm^2 and 20 Hz. Potassium was supplied from K_2O powder heated to 750 K in a tantalum-shielded MgO crucible. Growth rate was approximately 2.5 unit cells/min. Amorphous LaAlO_3 overlayers (3 nm) were deposited in situ at 673 K in 10^{-5} Torr using conventional PLD from a single crystal target. Structural quality was confirmed by X-ray diffraction and atomic force microscopy (Supplementary Fig. 1).

Compositional analysis

Nb concentrations were verified using field-emission electron probe microanalysis (FE-EPMA) with wavelength-dispersive spectroscopy. The Nb La peak position was calibrated using LiNbO_3 reference standards. Measurements employed 10 kV accelerating voltage, 400 nA beam current, and 20 μm spot size. X-ray intensities at the Nb La position increased systematically with nominal doping concentration (Supplementary Fig. 2).

Transport measurements

Electrical transport was measured using van der Pauw geometry from 2-300 K. Sheet resistance and Hall measurements employed DC current reversal to eliminate thermoelectric voltages. Carrier density was extracted from Hall slopes: $n_{2D} = 1/[(dR_H/dB)_e]$. Superconductivity measurements below 2 K utilized a dilution refrigerator with four-terminal configuration. Current-voltage characteristics employed current biasing through 300 $\text{k}\Omega$ series resistance. Zero-bias resistance used lock-in detection (10 nA, 13 Hz). High-field magnetoresistance up to 18 T was measured in a separate dilution system (Supplementary Fig. 3).

Device fabrication

Hall bars were patterned using photolithography and reactive ion etching. Gold alignment markers were first deposited. AZ4210 photoresist protected Hall bar regions during 18-minute $\text{BCl}_3/\text{Cl}_2/\text{Ar}$ plasma etching (100 W). Etching depth of 50 nm was confirmed by atomic force microscopy.

Supplementary information. Supplementary Information accompanies this paper.

Acknowledgements. Thin film synthesis at the University of Wisconsin–Madison was supported by the US Department of Energy (DOE), Office of Science, Office of Basic Energy Sciences (BES), under award number DE-FG02-06ER46327. CBE acknowledges support for this research through the Gordon and Betty Moore Foundation’s EPiQS Initiative, Grant GBMF9065 and a Vannevar Bush Faculty Fellowship (ONR N00014-20-1-2844). J.L. acknowledges NSF (DMR-2225888). Both C.B.E. and J.L. acknowledge ONR MURI (N00014-21-1-2537). We acknowledge helpful discussions with F. Yang and L. Q. Chen.

Author contributions. J.K. and C.B.E. conceived the project. C.B.E. and J.L. supervised the project. J.K. and J.Y. fabricated and characterized thin films. J.K., M.Y., A.O., and R.R. performed transport measurements. M.Y., A.O., and R.R. performed superconductivity measurements. W.N. performed compositional analysis. J.K., M.Y., J.L., and C.B.E. wrote the manuscript. All authors discussed results and commented on the manuscript.

Competing interests. The authors declare no competing interests.

Data availability. The data supporting the findings of this study are available from the corresponding authors upon reasonable request.

References

1. Hwang, H. Y. *et al.* Emergent phenomena at oxide interfaces. *Nat. Mater.* **11**, 103–113 (2012).
2. Ramesh, R. & Schlom, D. G. Creating emergent phenomena in oxide superlattices. *Nat. Rev. Mater.* **4**, 257–268 (2019).
3. Chen, Z. *et al.* Electric field control of superconductivity at the LaAlO₃/KTaO₃ (111) interface. *Science* **72**, 721–724 (2021).
4. Collignon, C., Lin, X., Rischau, C. W., Fauqué, B. & Behnia, K. Metallicity and Superconductivity in Doped Strontium Titanate. *Annu. Rev. Condens. Matter Phys.* **10**, 1–20 (2018).
5. Rowley, S. E. *et al.* Ferroelectric quantum criticality. *Nat. Phys.* **10**, 367–372 (2014).
6. Liu, C. *et al.* Two-dimensional superconductivity and anisotropic transport at KTaO₃ (111) interfaces. *Science* **371**, 716–721 (2021).
7. Liu, C. *et al.* Tunable superconductivity and its origin at KTaO₃ interfaces. *Nat. Commun.* **14**, 951 (2023).
8. Chen, Z. *et al.* Two-Dimensional Superconductivity at the LaAlO₃/KTaO₃ (110) Heterointerface. *Phys. Rev. Lett.* **126**, 026802 (2021).
9. Maryenko, D. *et al.* Superconductivity at epitaxial LaTiO₃-KTaO₃ interfaces. *APL Mater.* **11**, 061102 (2023).
10. Mallik, S. *et al.* Superfluid stiffness of a KTaO₃-based two-dimensional electron gas. *Nat. Commun.* **13**, 4625 (2022).
11. Arnault, E. G. *et al.* Anisotropic superconductivity at KTaO₃ (111) interfaces. *Sci. Adv.* **9**, eadfl414 (2023).
12. Islam, K. R. & Chubukov, A. Unconventional superconductivity near a nematic instability in a multi-orbital system. *npj Quantum Mater.* **9**, 28 (2024).
13. Lederer, S., Schattner, Y., Berg, E. & Kivelson, S. A. Enhancement of Superconductivity near a Nematic Quantum Critical Point. *Phys. Rev. Lett.* **114**, 097001 (2015).
14. Gegenwart, P., Si, Q. & Steglich, F. Quantum criticality in heavy-fermion metals. *Nat. Phys.* **4**, 186–197 (2008).
15. Shibauchi, T., Carrington, A. & Matsuda, Y. A Quantum Critical Point Lying Beneath the Superconducting Dome in Iron Pnictides. *Annu. Rev. Condens. Matter Phys.* **5**, 113–135 (2014).
16. Lee, P. A., Nagaosa, N. & Wen, X.-G. Doping a Mott insulator: Physics of high-temperature superconductivity. *Rev. Mod. Phys.* **78**, 17–85 (2006).

17. Edge, J. M., Kedem, Y., Aschauer, U., Spaldin, N. A. & Balatsky, A. V. Quantum Critical Origin of the Superconducting Dome in SrTiO_3 . *Phys. Rev. Lett.* **115**, 247002 (2015).

18. Uwe, H. & Sakudo, T. Stress-induced ferroelectricity and soft phonon modes in SrTiO_3 . *Phys. Rev. B* **13**, 271–286 (1976).

19. Höchli, U. T., Weibel, H. E. & Boatner, L. A. Quantum Limit of Ferroelectric Phase Transitions in $\text{KTa}_{1-x}\text{Nb}_x\text{O}_3$. *Phys. Rev. Lett.* **39**, 1158–1161 (1977).

20. Kim, J. *et al.* Electronic-grade epitaxial (111) KTaO_3 heterostructures. *Sci. Adv.* **10**, eadk4288 (2024).

21. Enderlein, C. *et al.* Superconductivity mediated by polar modes in ferroelectric metals. *Nat. Commun.* **11**, 4852 (2020).

22. Presland, M. R., Tallon, J. L., Buckley, R. G., Liu, R. S. & Flower, N. E. General trends in oxygen stoichiometry effects on T_c in Bi and Tl superconductors. *Phys. C: Supercond.* **176**, 95–105 (1991).

23. Hashimoto, M., Vishik, I. M., He, R.-H., Devereaux, T. P. & Shen, Z.-X. Energy gaps in high-transition-temperature cuprate superconductors. *Nat. Phys.* **10**, 483–495 (2014).

24. Hameed, S. *et al.* Enhanced superconductivity and ferroelectric quantum criticality in plastically deformed strontium titanate. *Nat. Mater.* **21**, 54–61 (2022).

25. Ahadi, K. *et al.* Enhancing superconductivity in SrTiO_3 films with strain. *Sci. Adv.* **5**, eaaw0120 (2019).

26. Russell, R. *et al.* Ferroelectric enhancement of superconductivity in compressively strained SrTiO_3 films. *Phys. Rev. Mater.* **3**, 091401 (2019).

27. Salmani-Rezaie, S., Jeong, H., Ahadi, K. & Stemmer, S. Interplay between Polar Distortions and Superconductivity in SrTiO_3 . *Microsc. Microanal.* **27**, 360–362 (2021).

28. Ren, X. *et al.* Possible strain-induced enhancement of the superconducting onset transition temperature in infinite-layer nickelates. *Commun. Phys.* **6**, 341 (2023).

29. Hosoi, S. *et al.* Nematic quantum critical point without magnetism in $\text{FeSe}_{1-x}\text{S}_x$ superconductors. *Proc. Natl. Acad. Sci.* **113**, 8139–8143 (2016).

30. Kumar, V. & Ganguli, N. Rashba-like spin-orbit interaction and spin texture at the KTaO_3 (001) surface from DFT calculations. *Phys. Rev. B* **106**, 125127 (2022).

31. Yoon, H. *et al.* Freestanding epitaxial SrTiO_3 nanomembranes via remote epitaxy using hybrid molecular beam epitaxy. *Sci. Adv.* **8**, eadd5328 (2022).

32. Schwaigert, T. *et al.* Molecular beam epitaxy of KTaO_3 . *J. Vac. Sci. Technol. A* **41**, 022703 (2023).

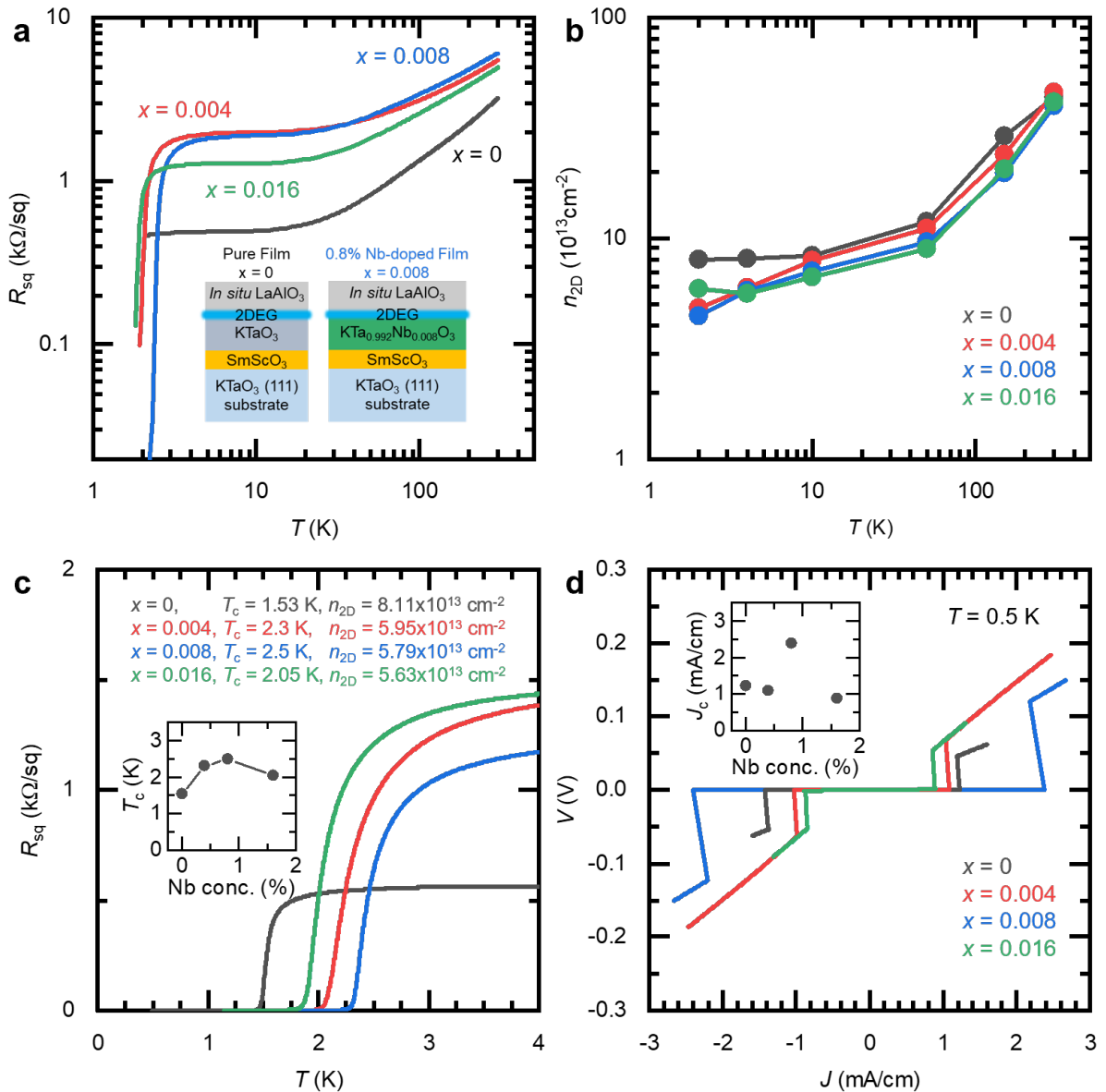


Figure 1 | Quantum critical enhancement of superconductivity. **a**, Temperature-dependent sheet resistance for different Nb concentrations. **b**, Carrier density remains comparable across samples. **c**, Superconducting transitions reveal maximum T_c at the quantum critical composition ($x = 0.8\%$). Inset: T_c versus doping concentration. **d**, Critical current density also maximizes at $x = 0.8\%$. Inset: Critical current versus doping.

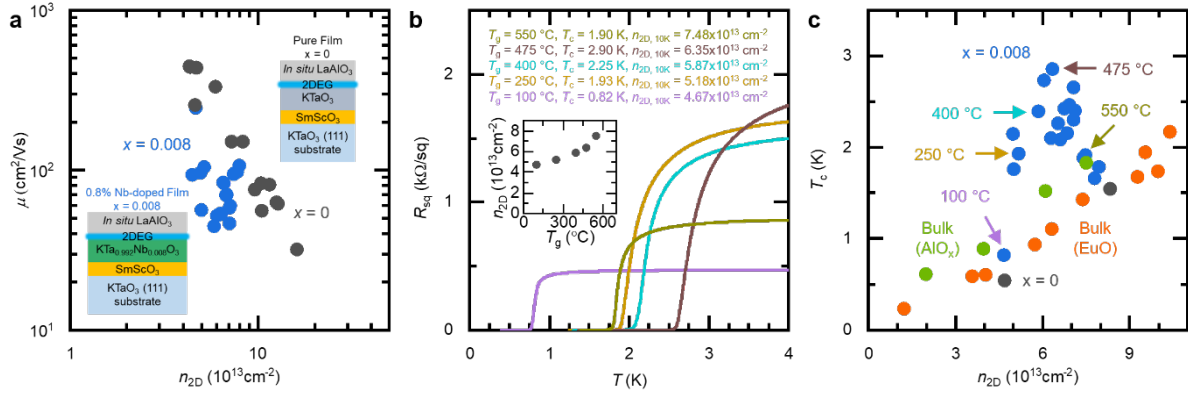


Figure 2 | Superconducting dome at the quantum critical point. **a**, Mobility and carrier density distributions for undoped (black) and quantum-critical (blue) interfaces. **b**, Superconducting transitions at different carrier densities. Maximum T_c of 2.9 K occurs at intermediate density. **c**, Systematic mapping reveals dome-shaped T_c dependence, contrasting with linear scaling in undoped samples. Bulk (EuO) is from C. Liu et al.⁷

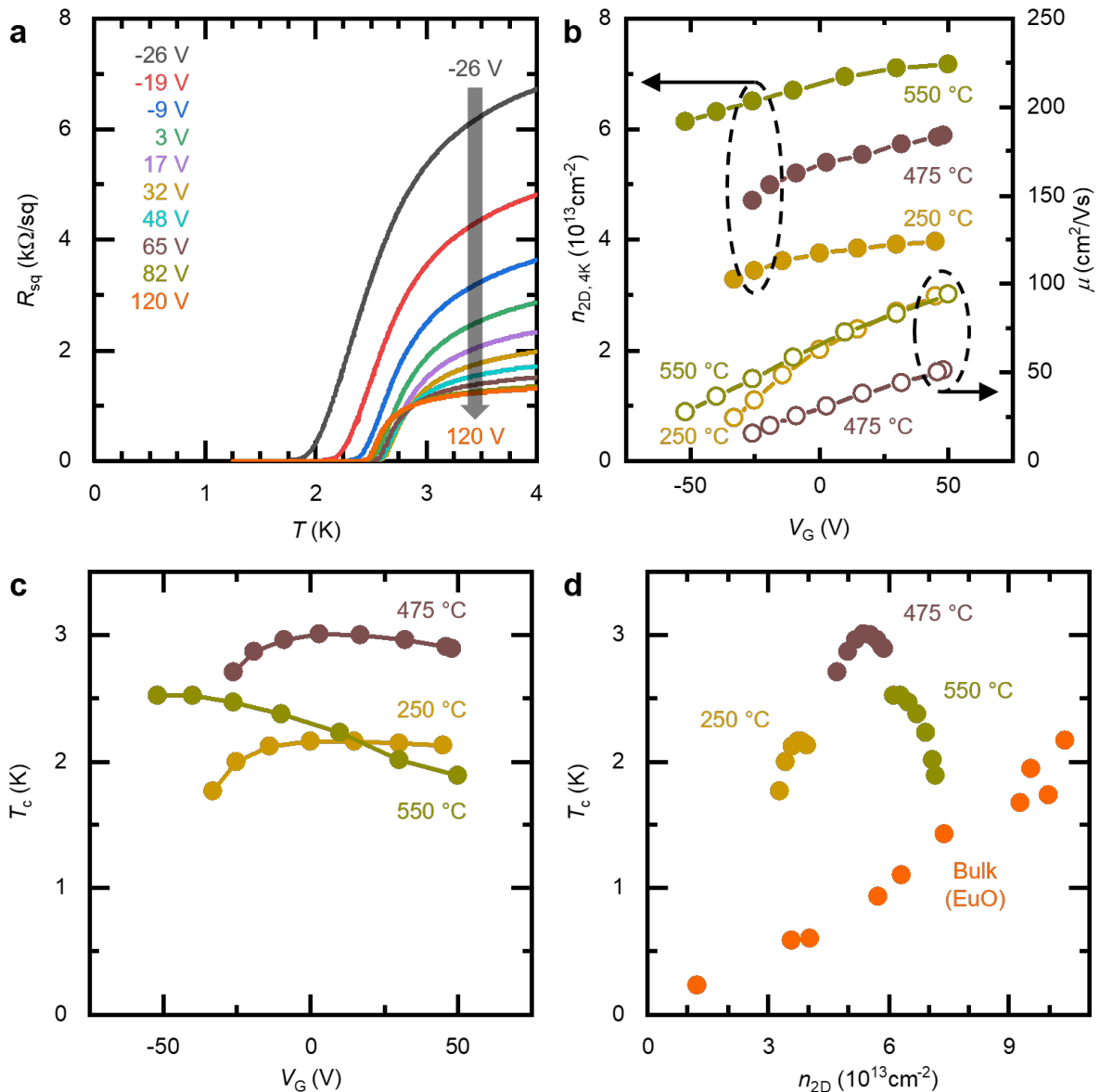


Figure 3 | Gate-tunable superconductivity confirms dome behavior. **a**, Electrostatic gating continuously tunes the superconducting transition. **b**, Gate voltage modulates carrier density and mobility. **c**, Non-monotonic T_c variation with gate voltage. **d**, Comprehensive phase diagram combining growth and gating experiments reveals sharp superconducting dome. Quantum critical enhancement (up to 3 K) dramatically exceeds both undoped interfaces and bulk superconductivity. Bulk (EuO) is from C. Liu et al.⁷

Supplementary Information

Enhanced Superconductivity at Quantum-Critical KTaO_3 Interfaces

Jieun Kim^{1,†}, Muqing Yu^{2,†}, Ahmed Omran², Jiangfeng Yang¹, Ranjani Ramachandran², William O. Nachlas³, Patrick Irvin², Jeremy Levy^{2,*} and Chang-Beom Eom^{1,*}

†These authors contributed equally to this work.

*Corresponding author(s). E-mail(s): jlevy@pitt.edu; ceom@wisc.edu;

This PDF file includes:

Supplementary Figures 1-4

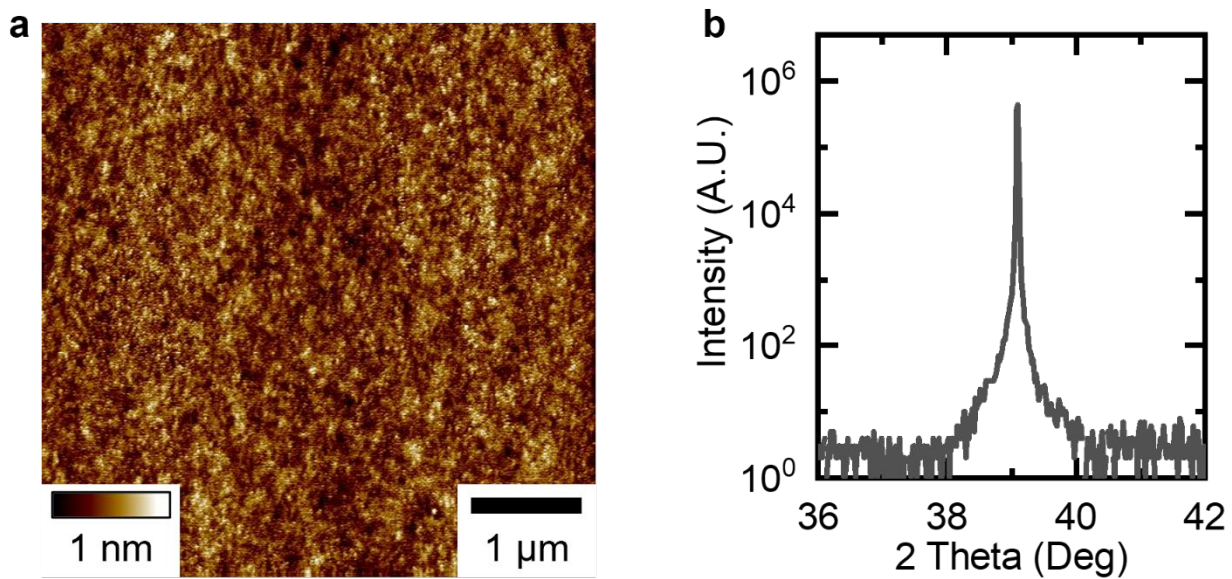


Fig. S1. Structural characterizations of $\text{KTa}_{0.992}\text{Nb}_{0.008}\text{O}_3/\text{KTaO}_3$ (111) heterostructures. a, Surface topography of ≈ 10 nm $\text{KTa}_{0.992}\text{Nb}_{0.008}\text{O}_3/\text{KTaO}_3$ (0111) heterostructures. **b,** θ - 2θ X-ray diffraction line scans of ≈ 10 nm $\text{KTa}_{0.992}\text{Nb}_{0.008}\text{O}_3/\text{KTaO}_3$ (0111) heterostructures

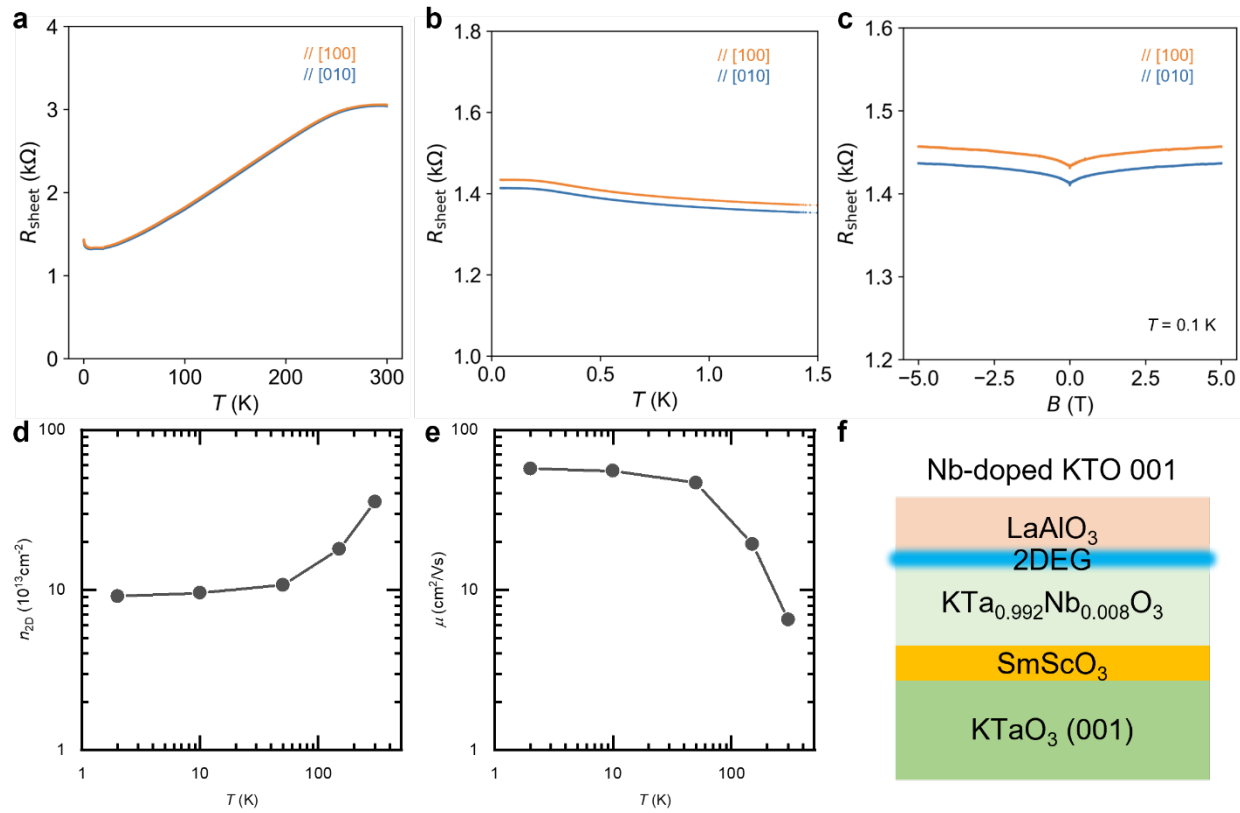


Fig. S2. Electrical transport properties of LaAlO₃ / KTa_{0.992}Nb_{0.008}O₃ (001) / SmScO₃ / KTaO₃ (001) heterostructures showing the absence of superconductivity down to ~50 mK. a, Temperature dependence of sheet resistance (R_{sheet}) from 300 to 2 K. b, Low-temperature R_{sheet} down to ~50 mK showing no superconducting transition. c, Magnetoresistance at $T = 0.1$ K up to 5 T, revealing no superconducting transition. d, Temperature dependence of carrier density (n_{2D}). e, Carrier mobility (μ) versus temperature. f, Schematic of the heterostructure.

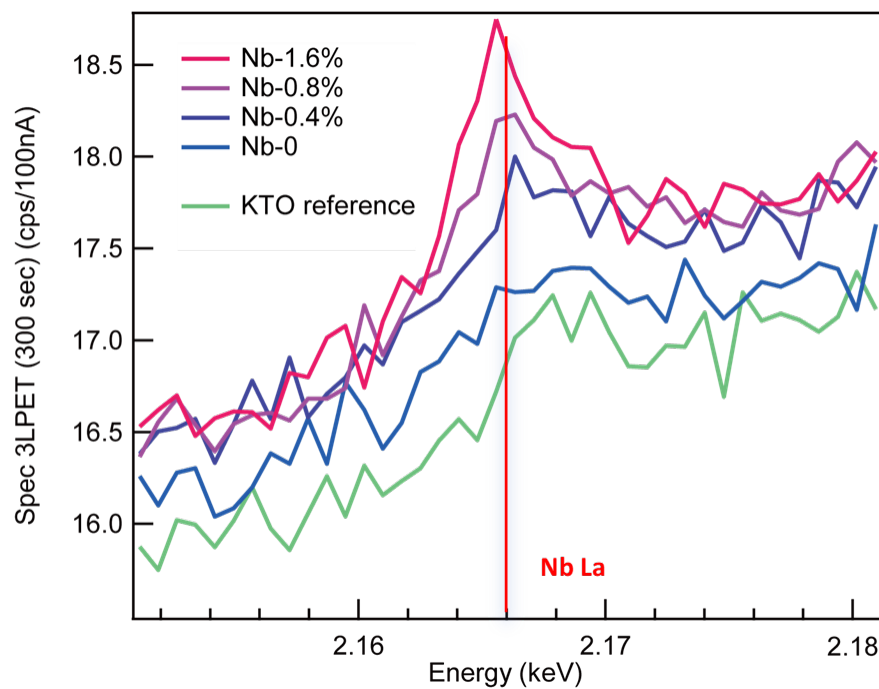


Fig. S3. Wavelength-dispersive spectroscopy (WDS) spectra of KTaO_3 reference crystal and Nb-doped KTaO_3 films (0, 0.4, 0.8, and 1.6% Nb)

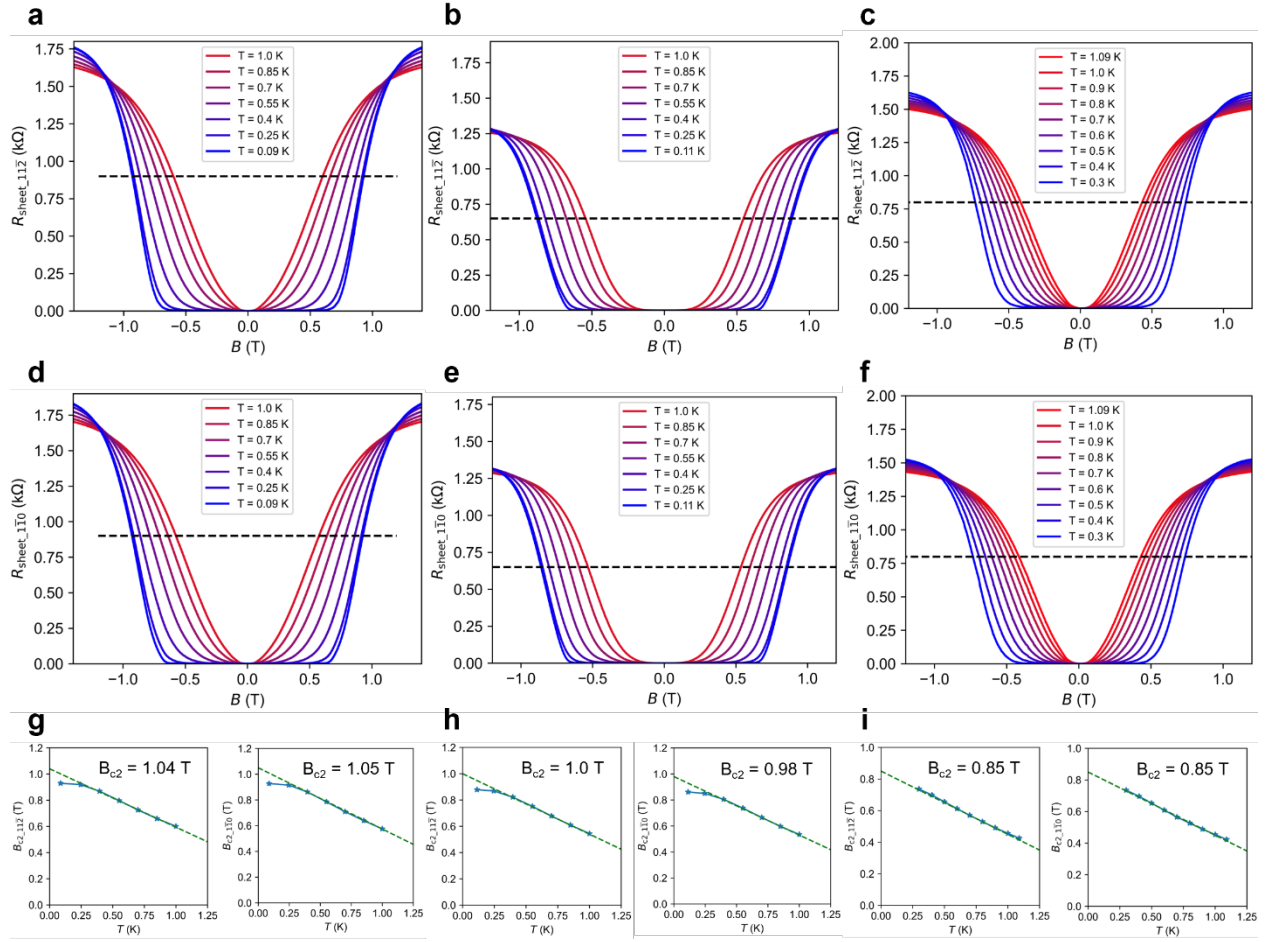


Fig. S4. Temperature-dependent magnetoresistance and extracted upper critical fields (B_{c2}) for Nb-doped KTaO_3 (111) two-dimensional superconductors. **a-c**, Sheet resistance (R_{sheet}) versus perpendicular magnetic field for devices patterned along the [11-2] direction with Nb doping levels of 0.4% (a), 0.8% (b), and 1.6% (c), measured at temperatures from 0.09 to 1.09 K. **d-f**, Corresponding R_{sheet} vs. B curves for Hall bars along the [1-10] direction with Nb doping levels of 0.4% (d), 0.8% (e), and 1.6% (f), measured at temperatures from 0.09 to 1.09 K. In a-f, dashed horizontal lines mark the 50% normal-state resistance criterion used to extract B_{c2} . **g-i**, Temperature dependence of B_{c2} for each device: 0.4% Nb along the [11-2] and [1-10] (g), 0.8% Nb along the [11-2] and [1-10] (h), and 1.6% Nb along the [11-2] and [1-10] (i).